Associated production of a top quark and a charged Higgs boson

Edmond L Berger,[1,*] Tao Han,[2,†] Jing Jiang,[1,‡] and Tilman Plehn[3,§]

[1]*High Energy Physics Division, Argonne National Laboratory, Argonne, Illinois 60439, USA*
[2]*Department of Physics, University of Wisconsin, Madison, Wisconsin 53706, USA*
[3]*CERN Theory Group, CH-1211 Geneva 23, Switzerland*

(Received 7 July 2004; published 28 June 2005)

We compute the inclusive and differential cross sections for the associated production of a top quark along with a charged Higgs boson at hadron colliders to next-to-leading order (NLO) in perturbative quantum chromodynamics (QCD) and in supersymmetric QCD. For small Higgs boson masses we include top-quark pair production diagrams with subsequent top-quark decay into a bottom quark and a charged Higgs boson. We compare the NLO differential cross sections obtained in the bottom parton picture with those for the gluon-initiated production process and find good agreement. The effects of supersymmetric loop contributions are explored. Only the corrections to the Yukawa coupling are sizable in the potential discovery region at the CERN Large Hadron Collider (LHC). All expressions and numerical results are fully differential, permitting selections on the momenta of both the top quark and the charged Higgs boson.

DOI: 10.1103/PhysRevD.71.115012 PACS numbers: 14.80.Cp, 13.85.Qk

I. INTRODUCTION

The elucidation of electroweak symmetry breaking is an important goal of particle physics. In the standard model, one neutral scalar Higgs boson is assumed to exist, and it is associated with the generation of the masses of the electroweak gauge bosons and of the fermions. The neutral Higgs boson has not yet been observed, and direct searches place a lower limit of about 114 GeV on its mass [1]. Extensions of the standard model include the possibility of more Higgs fields. The minimal supersymmetric standard model (MSSM) requires two doublets to give mass to up-type and down-type fermions and to cancel anomalies. The doublets yield five physical Higgs bosons: two neutral CP-even states, a CP-odd state, and a pair of charged scalars. At lowest order in perturbation theory, the masses and couplings of these states depend on two parameters which may be chosen as the pseudoscalar mass m_A and the ratio of the two vacuum-expectation values $\tan\beta = v_2/v_1$. Comprehensive analyses have been performed of the expected coverage of the $(\tan\beta, m_A)$ parameter space at the CERN Large Hadron Collider (LHC) [2]. While the observation of at least one of the two CP-even Higgs bosons may not pose a problem for the LHC [3], it will be challenging to distinguish it from its standard model counterpart over a large fraction of the parameter space. For small values of $\tan\beta$ the only viable channel in which to observe a heavy Higgs boson could be the resonant production of the scalar H with subsequent decay to $hh \to b\bar{b}\gamma\gamma$ [4], where b is a bottom quark. For large values of $\tan\beta$, the identification of a charged Higgs boson would provide evidence for a Higgs sector beyond the standard model, meaning at least two Higgs doublets, and possibly a supersymmetric Higgs sector.

If the charged Higgs boson is lighter than the top quark t, there is a good chance that it will be discovered via the decay channel $t \to bH^+$ in $p\bar{p}$ collisions at the Tevatron collider at 2 TeV, or in pp collisions at the LHC at 14 TeV. Searches in the Run I data samples by the CDF and D0 Collaborations at the Tevatron [5] place significant bounds on the mass m_H and $\tan\beta$. If the charged Higgs boson is heavier than the top quark, then its observation at hadron colliders becomes more problematic. In particular, there is no tree level coupling of a single charged Higgs boson to gauge boson pairs, and the production of $H^\pm$ is inaccessible in weak boson fusion. The cross section for H^+H^- pair production is likely to be too small, and the heavy quark backgrounds may be too large for the observation of charged Higgs boson pairs, unless additional supersymmetric particles enhance this loop-induced rate [6,7]. The situation is similar for the associated production of a charged Higgs boson with a W boson. The standard model leads to a fairly small rate, but supersymmetric particle loops might enhance the rate considerably [8,9].

The most promising search channel for a heavy $H^\pm$ is the associated production of a top quark and the charged Higgs boson $pp \to tH^- + X$ and $pp \to \bar{t}H^+ + X$ via the intermediary of a bottom-quark coupling [10]. Throughout this paper we present results only for the tH^- channel, unless stated otherwise. If both the tH^- and $\bar{t}H^+$ channels are included the rates increase by a factor of 2. Advanced detector simulation studies have been done for the decay channels $H^- \to \bar{t}b$ [11] and $H^- \to \tau\bar{\nu}$ [12]. The advantage of this production mode is that the Yukawa coupling to a top quark and a bottom quark is enhanced by a power of $\tan\beta$ for large values of $\tan\beta$, as are the bottom-quark Yukawa couplings of the heavy neutral Higgs bosons.

*Electronic address: berger@anl.gov
†Electronic address: than@pheno.physics.wisc.edu
‡Electronic address: jiangj@hep.anl.gov
§Electronic address: tilman.plehn@cern.ch

We consider the leading-order partonic subprocess to be

$$gb \to tH^-, \tag{1}$$

with the initial-state bottom quark taken as a constituent of an incident proton. The set of next-to-leading-order subprocesses includes partonic reactions such as $gg \to \bar{b}tH^-$. The total rate for the process $pp \to \bar{b}tH^- + X$ receives large corrections from collinear logarithms, originating from the radiation of a forward bottom-quark jet [13,14]. These logarithmic terms can be resummed to all orders in the strong coupling strength α_s, leading to the bottom parton picture [13] with an appropriate bottom-quark factorization scale [14–16]. This resummation of large collinear logarithms is valid not only for charged Higgs boson production, but it is generic as long as there is a large mass scale M that provides $\log(M/p_{T,b})$ behavior. In our case $M = m_t + m_H$. The comparison of higher order predictions for total cross sections of neutral Higgs boson production shows impressive agreement between gluon-initiated and bottom parton results [17,18], but the absence of a heavy scale in neutral Higgs boson production in association with bottom quarks may have an impact on some final-state distributions.

The tH^- production cross section can be evaluated with or without integration over the phase space of the final-state bottom quark, corresponding to whether an accompanying final-state bottom quark is observed or ignored. The term ''exclusive'' is generally used to refer to a situation in which the final-state bottom quark is observed, and ''inclusive'' is used to refer to the case in which the final-state bottom quark is ignored.

Calculations of the next-to-leading order (NLO) total cross section for $pp \to tH^- + X$ are available in perturbative quantum chromodynamics (QCD) [14,19] as well as in supersymmetric QCD [14,20]. If we use the same choice of parameters, most importantly the same renormalization and factorization scales, and the same scheme for renormalization for the Yukawa couplings, our numerical results are in good agreement with those of Ref. [19]. We comment in greater detail in Sec. II C about the differences in scheme choice. The inclusion of NLO contributions to the gb initial-state process merges the ''inclusive-type'' process $gb \to tH^-$ with the ''exclusive-type'' process $gg \to \bar{b}tH^-$, whose contribution appears as part of the set of NLO diagrams. The NLO contributions increase the reliability of the theoretical predictions by reducing the renormalization and factorization scale dependence of the total rate.

In this paper, we present fully differential NLO cross sections for the process $gb \to tH^-$. The differential distributions are desirable, as are predictions of expected correlations among the final-state observables, since selections on final-state kinematic variables must be made in experimental studies, for reasons of event acceptance and background rejection. In Sec. II, we outline the two-cutoff phase-space slicing method which we adopt. We then study the NLO production rates at the LHC and the Tevatron with the associated theoretical uncertainties. We present typical kinematic distributions and momentum correlations in Sec. III. For searches in the framework of the MSSM we examine the effects of leading and subleading supersymmetric QCD corrections in Sec. IV. Conclusions are summarized in Sec. V.

The results in this paper go beyond those of Refs. [14,19] in several respects. The calculation presented in Ref. [14] uses a one-cutoff method for NLO calculations. The two-cutoff method in this paper permits a fully differential treatment of the final-state particles. In this paper, we show that the bottom parton approach is justified for *differential* cross sections as well as for total cross sections. A more extensive discussion of cutoff dependences is presented in this paper including two-dimensional plots. In our treatment of SUSY-QCD corrections in Sec. IV, we include an evaluation for the Snowmass points and slopes (SPS) parameters and the impact of resummation of the Δ_b corrections. Going beyond Ref. [19], we include SUSY-QCD corrections, and an exploration of the interplay of bottom parton and gluonic contributions. The matching of cross sections for small charged Higgs boson masses is new. Matching near the top decay threshold is of considerable interest for LHC experiments.

II. NEXT-TO-LEADING-ORDER QCD CORRECTIONS

Throughout the paper we use a running strong coupling α_s, a bottom-quark Yukawa coupling y_b, and a top-quark Yukawa coupling y_t consistent with the order of perturbation theory, i.e., one-loop running for the leading order and two-loop running for the next-to-leading-order results. If not stated explicitly otherwise we neglect the bottom-quark mass m_b in the phase space as well as in the matrix elements, while naturally keeping it in the bottom-quark Yukawa coupling. The Yukawa coupling is normalized to $m_b(m_b) = 4.2$ GeV and a bottom-quark pole mass of 4.6 GeV. Moreover, we use the CTEQ5 parton densities [21]. We refer to the K factor defined by $K = \sigma_{\rm NLO}/\sigma_{\rm LO}$, the ratio of the NLO cross section over the leading-order cross section. The default choices of the renormalization scale and the factorization scale are taken to be proportional to the hard scale in the process [14,15]

$$\mu_R^0 = M/2, \qquad \mu_F^0 = M/5 \qquad (M = m_H + m_t). \tag{2}$$

A detailed explanation of these choices may be found in Sec. II B.

At leading order in QCD we start from the parton-level production process in Eq. (1), with the diagrams depicted in Fig. 1. It is appropriate to define the bottom quark as a parton at high energies since the Dokshitzer-Gribov-Lipatov-Altarelli-Parisi (DGLAP) evolution equation [22]

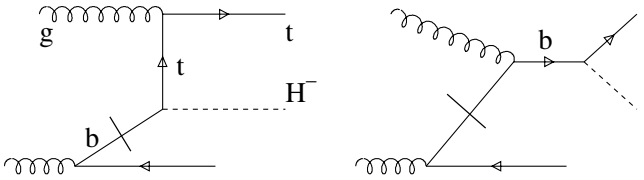

FIG. 1. The leading-order Feynman diagrams for the production process $gb \to tH^-$. We indicate how the bottom partons are created through gluon splitting.

resums large logarithmic $\log p_{T,b}$ contributions from small $p_{T,b}^{\min} \sim m_b$ to a maximum value $p_{T,b}^{\max}$ (which in turn determines the b-quark factorization scale). The bottom parton density is therefore not suppressed by a simple power of α_s. The leading-order cross section for a process involving one incoming bottom parton and an incoming gluon is of the order of $\alpha_s y_{b,t}^2$, where $y_{b,t}$ is the bottom-top-Higgs Yukawa coupling. If $y_{b,t}$ is written as $y_{b,t}^2 = y_t^2 + y_b^2$, y_t and y_b are terms proportional to $(m_t/\tan\beta)$ and $(m_b \tan\beta)$ respectively. For large values of $\tan\beta$, $y_{b,t}$ is dominated by y_b. The validity of our choice of the process in Eq. (1) as the leading contribution is confirmed by our numerical results, namely, that the perturbative series is well behaved over a wide range of scales.

There are two classes of NLO contributions:

(i) Virtual gluon exchange corrections to the lowest order process and the corresponding real gluon emission corrections, both of order $\alpha_s^2 y_{b,t}^2$

$$\begin{aligned} &gb \to tH^- \qquad \text{(virtual correction)}, \\ &gb \to tH^- g. \end{aligned} \tag{3}$$

(ii) The purely gluon-initiated and the purely quark-initiated diagrams, which lead to cross sections also of the order $\alpha_s^2 y_{b,t}^2$,

$$\begin{aligned} &gg,\, q\bar{q},\, b\bar{b} \to tH^-\bar{b}, \qquad bb \to tH^- b, \\ &\qquad b\bar{q} \to tH^-\bar{q}, \qquad bq \to tH^- q. \end{aligned} \tag{4}$$

Because we neglect the bottom-quark mass in the phase space and in the matrix elements, the purely gluon and purely quark-initiated subprocesses are divergent in the collinear limit. In our calculation these divergences are removed through mass factorization, i.e. the proper definition of all parton densities at NLO.

One may think about an alternative treatment of the associated production process, namely, to start with the process $gg \to tH^-\bar{b}$ as the leading contribution. These diagrams are part of the α_s correction to the bottom-gluon fusion process. For a choice of the factorization scales $\mu_{F,g} = \mu_{F,b} \to m_b$ the bottom parton density vanishes, in contrast to the gluon density, which is stable and well defined down to scales of the order of $\Lambda_{\rm QCD}$. In a physical picture of this limit we consistently switch off all large collinear logarithmic contributions, because $p_{T,b}^{\max} \equiv \mu_{F,b}$. We are then left with only the purely light-flavor $q\bar{q}$ and gg induced processes listed in Eq. (4). We use this limit of a small bottom-quark factorization scale in Sec. III to check the impact of the bottom parton picture on the final-state differential cross sections.

A. Phase-space slicing

One of the main tasks of our calculation is to integrate the three-body matrix elements over the phase space of the unobserved particle in the final state. The situation is different from the case of the single particle inclusive calculation in which one integrates over the phase space of two particles in the final state. We wish to retain control over the kinematic variables of a second particle in the final state, while at the same time integrating over enough of the phase space to ensure cancellation of all infrared and collinear divergences. Several techniques have been introduced for these purposes. The phase-space slicing [23,24] and the subtraction methods [25] are two ways to extract the singularities in the real emission contributions as exclusively as possible. All relevant information needed to compute a $2 \to 2$ particle NLO cross section with the two-cutoff slicing method is compiled in Ref. [24]. We follow this description closely in our calculations.

The ultraviolet divergences in the virtual $2 \to 2$ corrections are handled with dimensional regularization. The heavy final-state masses are renormalized in the on-shell scheme, while all couplings—the strong coupling as well as the bottom-quark and the top-quark Yukawa couplings—are renormalized in the $\overline{\rm MS}$ scheme. The mismatch of the prefactors between the virtual corrections and the counter terms leads to the usual explicit $\log\mu_R$ dependence of the NLO cross section on the renormalization scale. The choice of the renormalization scale μ_R and that of the factorization scale μ_F are discussed in Sec. II B.

Virtual gluon exchange and real parton emission lead to both soft and collinear divergences. They are extracted with dimensional regularization and partially canceled with each other and partially removed through mass factorization, i.e. the consistent definition of parton densities. The situation is relatively simple for processes that have different initial states from the leading-order gb case because no soft divergence appears. Schematically, we can write the contributions arising from the processes in Eq. (4) as

$$d\sigma_q = d\sigma_{2\to3,q}^{\rm HC} + d\sigma_{2\to3,q}^{\rm finite} + d\sigma_q^{\rm HMF}. \tag{5}$$

The label HC indicates hard-collinear divergences, which cancel with the universal contributions from hard mass factorization (HMF). The collinear phase-space region, which appears for all $2 \to 3$ kinematics, is defined as the region in which the value of the corresponding invariant for the two possibly collinear momenta p_i and p_j falls below

$(p_i + p_j)^2 < \delta_c s$, where $\sqrt{s}$ is the partonic center of mass energy. The squared matrix element is finite in the noncollinear phase-space region and can be integrated numerically, creating an implicit logarithmic dependence on the cutoff δ_c. Applying the hard mass factorization corrections, we subtract the hard-collinear contributions as a convolution of the leading-order matrix element and the appropriate finite splitting function, multiplied by $\log\delta_c$ [24]. The mismatch of prefactors leads to an additional explicit dependence of the NLO cross section on the factorization scale $\log\mu_F$.

The situation for virtual and real gluon emission in the gb initial state is slightly more involved because additional divergences appear due to soft-gluon emission. Soft-gluon emission is defined by the noninvariant gluon energy constraint $E_g < \delta_s\sqrt{s}/2$. The cross section can be written as

$$d\sigma_g = d\sigma^{\mathrm{S}}_{\mathrm{virt}} + d\sigma^{\mathrm{SC}}_{\mathrm{virt}} + d\sigma^{\mathrm{S}}_{2\to3} + d\sigma^{\mathrm{SC}}_{2\to3} + d\sigma^{\mathrm{SMF}} + d\sigma^{\mathrm{HC}}_{2\to3,g} + d\sigma^{\mathrm{finite}}_{2\to3,g} + d\sigma^{\mathrm{HMF}}_{g}, \quad (6)$$

where the label S means soft, SC soft-collinear, and SMF soft-mass-factorization. The additional soft $1/\epsilon$ and overlapping soft-collinear $1/\epsilon^2$ divergences appear in the virtual corrections as well as in the real gluon emission corrections. The divergences cancel among the virtual correction, the real gluon emission correction, and the contributions from mass factorization. We integrate numerically over the hard and noncollinear part of phase space and obtain an implicit dependence on $\log\delta_s$ and $\log\delta_c$.

No explicit scale dependence occurs in dimensional regularization after the purely soft divergences are canceled between the different $d\sigma^{\mathrm{S}}$ and $d\sigma^{\mathrm{SC}}$ contributions, and the prefactors between real and the virtual gluon emission diagrams are matched. All poles in $d\sigma^{\mathrm{S}}$ and all double poles in $d\sigma^{\mathrm{SC}}$ vanish after the soft divergences are removed, and only single collinear poles $1/\epsilon$ remain in $d\sigma^{\mathrm{SC}}$. Cancellation of these remaining divergences with the soft-mass-factorization contribution renders a finite virtual gluon emission matrix element with an additional explicit dependence on $\log\delta_s$. This logarithmic dependence cancels against the implicit dependence of the numerically integrated hard noncollinear phase space. An explicit dependence on the factorization scale $\log\mu_F$ remains in the universal mass factorization terms. Last, as a slight complication, the same soft-collinear phase-space configurations, which include an explicit $\log\delta_c$ factor, also lead to an implicit $\log\delta_s$ dependence after the numerical phase-space integration. This dependence again cancels with the cutoff dependence of the $2 \to 3$ phase space, but it makes the numerical analysis tedious [24].

Both cutoff parameters, δ_s and δ_c, must be small in order that the soft and collinear approximation of the universal terms be valid. Physical observables should not depend on the cutoff parameters appreciably. We have checked in detail that the NLO cross section and the distributions approach a two-dimensional plateau for sufficiently small values of δ_s and δ_c. To define the soft and the collinear regions of phase space consistently and to avoid double counting, it is most convenient to require $\delta_c \ll \delta_s$ and then determine the one dimensional plateau for a fixed relation between δ_s and δ_c. We show the behavior of the cross section versus the soft and the collinear cutoffs in Fig. 2 at the LHC energy. The cross section develops a wide plateau for $\delta_c \lesssim \delta_s$. Unless noted otherwise we use $\delta_c = 10^{-5}$ and $\delta_s = 10^{-3}$ in all numerical analyses. Checking the two-dimensional plateau and comparing it with results for the total cross section obtained with a one-cutoff method [14], we find that the NLO cross section has a remaining uncertainty of 0.1%–0.5% due to the cutoff dependence and the corresponding numerical uncertainty.

B. Scale Dependence

Perturbative QCD calculations introduce an unwelcome dependence on the renormalization scale μ_R and the factorization scale μ_F. One of the major motivations to perform NLO calculations is to reduce this scale dependent theoretical uncertainty in predictions of physical observables. As the default renormalization scale, we choose Eq. (2), related to the hard scale M. We identify the renormalization scales of the strong coupling and the Yukawa coupling. This central renormalization scale choice leads to pertur-

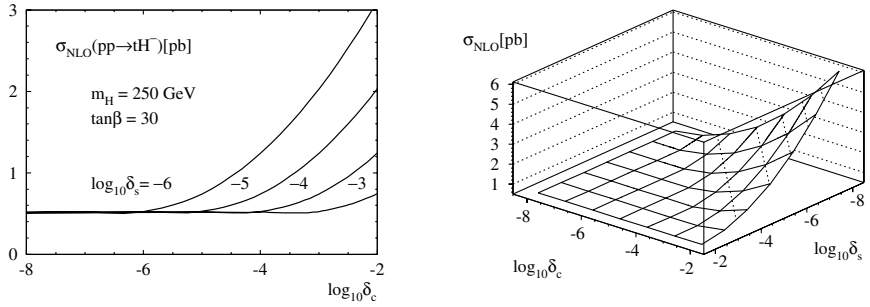

FIG. 2. Cross section dependence on the cutoff parameters δ_c and δ_s at the LHC energy. Left: The soft cutoff δ_s is fixed to different values. Right: two-dimensional logarithmic dependence on both cutoff parameters.

batively stable predictions for cross sections and branching fractions as functions of α_s [26,27] and as functions of y_b [28]. The situation is different for the factorization scale. Two reasons point to a central scale considerably smaller than the hard scale M, an optimum choice being $\mu_F = M/5$.

First, we can estimate the factorization scale from the kinematics of the process $gg \to \bar{b}tH^-$. The bottom-quark factorization scale may be defined as the maximum $p_{T,b}$ which is included in the $2 \to 2$ $gb \to tH^-$ process. For the perturbatively calculated bottom-quark density we can go back to the process $gg \to \bar{b}tH^-$ and estimate up to which value $p_{T,b}^{\max}$ the cross section shows the asymptotic behavior $\sigma_{\bar{b}tH^-} \sim 1/p_{T,b}$. The hadronic phase space or, more specifically, the gluon luminosity cuts off the asymptotic behavior near $p_{T,b}^{\max} \sim M/5$. This behavior can be understood independently from the form of the matrix element, as long as both incoming partons are either gluons or bottom quarks [14,15]. From basic principles it is not clear if one could use the (factorizing) internal momentum transfer Q_b instead of $p_{T,b}$ [16]. The difference in the maximum value up to which the asymptotic form holds is $p_{T,b}^{\max} \sim Q_b^{\max}/2$, and the plateau in $p_{T,b}$ is considerably softened [15]. We take this uncertainty into account by varying the factorization scale over a generous range. Our argument works because the bottom parton density is calculated perturbatively, meaning that its features are well defined and understood perturbatively.

Second, in the similar LHC process $b\bar{b} \to h$, the explicit next-to-next-to-leading-order (NNLO) corrections are perturbatively most stable for, and therefore point to, the same small factorization scale [18]. Moreover, the NLO corrections to the similar process $b\bar{b} \to W^+H^-$ are negative for $\mu_F = M$ [9], indicating possibly a collinear subtraction much too large.

The variation of the total cross section with the factorization and renormalization scales is under control perturbatively if the two scales μ_R and μ_F are varied independently [14]. However, there is a very large shift in the total rate if the two scales are varied together $\mu_R \propto \mu_F$ and run to very small values $\mu \lesssim M/10$. This behavior suggests the presence of large contributions proportional to $\log\mu_R \times \log\mu_F$. In Fig. 3 we show the scale dependence of the different contributions to the leading-order and next-to-leading-order cross sections for the process $gb \to tH^-$. The leading-order curve (upper-left) behaves as one would expect, namely, the cross section increases for small μ_R and for large μ_F, independently of each other. This behavior arises from the running strong coupling α_s and the bottom parton distribution. In contrast, the running bottom Yukawa coupling is relatively constant for these large scales. The NLO gb initiated curve (lower-left) is also easy to understand. The cross section increases with the (bottom-quark) factorization scale, but it develops a maximum as a function of μ_R at a physical value of the scale, for values of μ_F not too large. The fraction $\sigma_{\mathrm{NLO},gb}/\sigma_{\mathrm{LO}}$ is under control perturbatively over the range of scales, varying at most 20%. The corrections are largest (and negative) for small μ_R, because α_s is largest there. Comparison of the NLO and LO results in the OS scheme with those obtained in the $\overline{\mathrm{MS}}$ scheme shows that use of the bottom-quark pole mass as the Yukawa coupling produces perturbatively less stable rates, giving an unacceptably large leading-order cross section. The $gg \to \bar{b}tH^-$ contribution

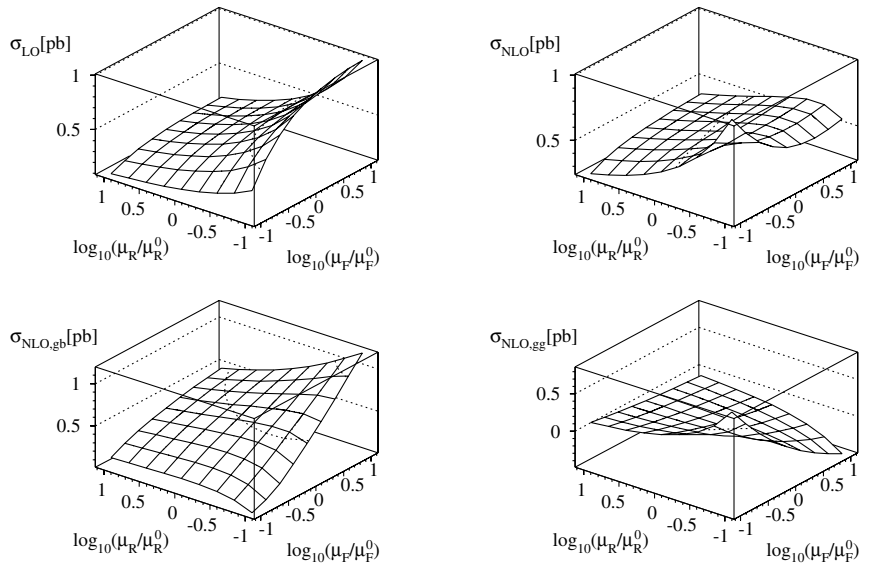

FIG. 3. The scale variation of the cross sections at the LHC for $m_H = 250$ GeV and $\tan\beta = 30$. The central values are $\mu_R^0 = M/2$ and $\mu_F^0 = M/5$. The four panels show the leading-order cross section, the complete NLO cross section, the gb induced NLO cross section and the gg induced contribution to the NLO cross section.

(lower-right) to the NLO rate has a very different behavior, which dominates the complete NLO rate. The gg contribution is regulated through mass factorization, meaning that we compute this process by subtracting out the contribution which is included in the collinear bottom-quark splitting. For a central $\mu_R \sim \mu_R^0$, the gg channel gives a small positive contribution for small μ_F and a small negative contribution for large μ_F. The latter indicates that a choice of a large scale overestimates the logarithmic terms, an overestimate then corrected by the explicit NLO diagram. If we do not take into account the difference in size of the gluon and bottom parton luminosities, the gg initiated process is suppressed by a factor α_s as compared to the gb process. The pattern of correcting behavior stays but becomes much steeper if we decrease μ_R and thereby increase α_s. For a central value $\mu_F \sim \mu_F^0$ the gg initial-state corrections are zero, and for much larger or smaller μ_F their absolute value increases sharply. The gg contribution grows for small μ_F and simultaneously small μ_R. This effect can be rationalized if we take the position that the choice of very small μ_F and very small μ_R corresponds to a region in parameter space where the gb initial state is not dominant perturbatively. The result arises because we choose to ignore the presence of large collinear logarithms up to $p_{T,b}^{\max} \equiv \mu_{F,b}$ and at the same time we push α_s to large values. The K factor grows, indicative that we should use the process $gg \to \bar{b}tH^-$ as the leading process.

C. Total cross section at the LHC

The effects of the NLO corrections on the total cross sections for the process $gb \to tH^-$ at the LHC are shown in Fig. 4, versus $\tan\beta$ and versus the charged Higgs boson mass m_H. The solid curve shows the NLO cross section, with the scale variations around the central scale $\mu/\mu_0 = 1/4 - 4$ indicated by the thin solid lines in the left panel. The total cross section increases for large values of $\tan\beta$, as expected for the leading behavior $\sigma_{\rm tot} \propto \tan^2\beta$, while the K factor is fairly independent of $\tan\beta$ [14]. At leading order we compare the cross section predictions for running bottom-quark Yukawa coupling and the pole-mass Yukawa coupling. The pole-mass Yukawa coupling overestimates the total production rate, while the leading-order rate with a running bottom-quark Yukawa coupling is a more reasonable approximation. With the running bottom-quark Yukawa coupling, the NLO result is slightly enhanced by a factor of $K \sim 1.4$ [14]. The scale variation suggests a remaining theoretical uncertainty of about 20% on the predicted NLO cross section. Both results confirm that the perturbative behavior of the production process $gb \to tH^-$ is under control.

In the right panel of Fig. 4, the NLO and LO cross sections are indicated by the dashed upper and lower curves, respectively. The size of the NLO corrections is essentially independent of the Higgs boson mass, a uniform enhancement factor of about 1.4. The process $gb \to tH^-$ itself is well defined over the entire range of Higgs boson masses, as long as the hard scale $M = m_H + m_t$ is sufficiently large to motivate the bottom parton picture.

An interesting region is one in which the Higgs boson mass becomes similar to or smaller than the top-quark mass, and the decay $t \to bH^-$ is possible. In Fig. 4 we see that the production of a top-quark pair $pp \to t\bar{t} + X$ with subsequent (off-shell) decay $\bar{t} \to \bar{b}H^-$ becomes the dominant process. For $m_H \lesssim m_t$ the production cross section is of order $\alpha_s^2 y_{b,t}^2$ instead of $\alpha_s y_{b,t}^2$, and the large gluon luminosity at the LHC is effective in this range of partonic energy. In the following we discuss how these two processes can be combined, to obtain a prediction of the cross section over the entire range of Higgs boson masses.

For small Higgs boson masses, below the threshold $\bar{t} \to \bar{b}H^-$, the $t\bar{t}$ production process with a subsequent decay of the $\bar{t}$ dominates the rate for associated production of a charged Higgs boson. It is straightforward to combine the $t\bar{t}$ production process and the exclusive production channel $pp \to \bar{b}tH^- + X$ with a tagged final-state bottom-quark jet [29]. We compute the process $pp \to \bar{b}tH^- + X$ with a finite top-quark width, essentially giving us a Breit-Wigner

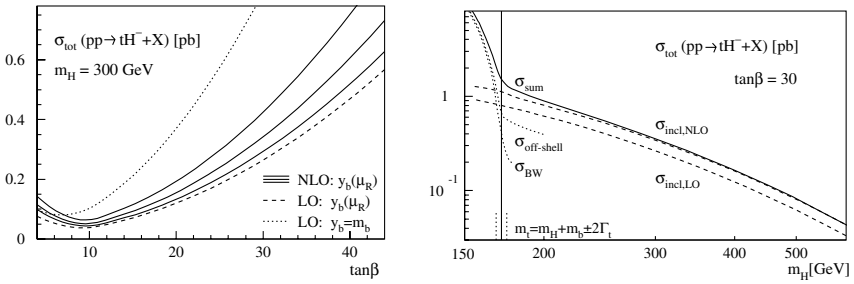

FIG. 4. Left: The tH^- inclusive cross section at the LHC as a function of $\tan\beta$. The solid curve is the NLO result, with the scale variations around the central scale $\mu/\mu_0 = 1/4 - 4$ indicated by the thinner solid curves. Also shown are the leading-order result with a running bottom-quark Yukawa coupling (dashed curve) as well as a pole-mass Yukawa coupling (dotted curve). Right: The total cross section at the LHC as a function of the charged Higgs boson mass as the solid curve. The NLO and LO cross sections are shown as the dashed upper and lower curves, respectively. The dotted curves show the cross sections for $pp \to t\bar{t}^* + X$ with a subsequent decay $\bar{t} \to \bar{b}H^-$ in the Breit-Wigner approximation ($\sigma_{\rm BW}$) and that including the complete set of off-shell diagrams ($\sigma_{\text{off-shell}}$).

propagator for the intermediate $\bar{t}$. Approximate gauge invariance can be achieved in the overall factor scheme [30], in which additional terms $\mathcal{O}(\Gamma_t/m_t)$ are traded for a gauge invariant matrix element. Referring to the dotted curves in the right panel of Fig. 4, we see that the process $\bar{t} \to \bar{b}H^-$ is approximated well by the subset of diagrams with an intermediate $\bar{t}$ in the Breit-Wigner approximation, as long as the Higgs boson mass is below the top-quark threshold. Above the top-quark threshold, the exclusive process $pp \to \bar{b}tH^- + X$ is dominated by the continuum off-shell diagrams, i.e. the off-shell extension of the $t\bar{t}$ production process, including all the diagrams initiated from $q\bar{q}$ and gg. These off-shell diagrams become dominant where the cross section flattens and settles below the gb rate, while the Breit-Wigner cross section becomes very small.

For Higgs boson masses above threshold, a bottom-quark jet tag is a heavy price to pay, and it is likely a better idea to consider the bottom-inclusive process. The collinear logarithms become large, and to obtain the best possible prediction of the rate we must compute the process $gb \to tH^-$ [14], keeping in mind that even at threshold the hard scale of the process is $M = 350\ \text{GeV} \gg m_b$. The difference between the bottom-gluon induced rate and the off-shell curve in Fig. 4 shows this enhancement of the rate due to the resummed logarithmic terms. Strictly speaking, we should take into account that off-shell production also includes the quark-initiated channels $q\bar{q} \to \bar{b}tH^-$, which do not contribute to the bottom parton density at leading order. However, they contribute only about 10% to the total exclusive rate. The matching of the regions of small and large Higgs boson mass in Fig. 4 indicates that a combination is needed of the $t\bar{t}$ production process with the process $gb \to tH^-$. There appears to be no region of Higgs boson masses where the off-shell production process $gg \to \bar{b}tH^-$ is the appropriate perturbative description.

In Fig. 4 we show the different $t\bar{t}$ cross sections with a finite bottom-quark mass, while we neglect the bottom-quark mass for the gb channel. The uncertainty induced by this approximation is small, however, since we cannot avoid neglecting Γ_t/m_t corrections and $m_b/M \sim \Gamma_t/M$.

At leading order the Breit-Wigner approximation of the $pp \to t\bar{t}^* + X$ process, with subsequent decay of the off-shell $\bar{t}^*$, may be combined without problems with the process $gb \to tH^-$. We may add the independent event samples for any Higgs boson mass value. However, at NLO and for Higgs boson masses smaller than the top-quark mass there is a potential problem of double counting. The $t\bar{t}^*$ production process with a subsequent decay of the $\bar{t}^*$ can be regarded as an $\mathcal{O}(\alpha_s)$ correction to the gb initiated process, Eq. (4), while it can as well be viewed as (nearly) on-shell $t\bar{t}$ production with a subsequent decay $\bar{t} \to \bar{b}H^-$. To avoid double counting, we subtract the resonant on-shell part of the $t\bar{t}$ diagrams from the NLO correction to tH^- production and keep it as part of the $pp \to t\bar{t} + X$ rate. The nondivergent off-shell contribution of the $\bar{t}^*$ propagator is counted toward the NLO tH^- rate. The division into on-shell and off-shell contributions, however, is well defined only in the narrow width approximation, so we neglect terms of order Γ_t/m_t. The ambiguity reflects the unsolved problem of how a long-lived intermediate particle is treated in field theory. Up to finite width corrections we can, just as at leading order, add the rate for $t\bar{t}$ production with a Breit-Wigner propagator and the properly subtracted NLO $gb \to tH^-$ rate to obtain a prediction for any given Higgs boson mass. In Fig. 4 we see that addition of the cross sections is essentially equivalent to a naive matching procedure. It is perhaps unexpected that the corrections from the Breit-Wigner propagator extend to large Higgs boson masses. On the other hand, since there is a $\sim$20% [14] theoretical uncertainty on the NLO cross section for the gb induced process, the details of this matching/adding procedure are not important phenomenologically. Instead of including the on-shell production with the Breit-Wigner propagator for Higgs boson mass values above 300 GeV, we could as well have cut it off at $m_H \simeq m_t + 10\Gamma_t$.

Below the $\bar{t} \to \bar{b}H^-$ threshold, the Breit-Wigner description is valid, with higher order contributions included in the cross section for $pp \to t\bar{t} + X$ [31,32]. Off-shell effects have little impact there. Above threshold these off-shell effects have a considerable impact relative to the Breit-Wigner description, but the $gb \to tH^-$ cross section is dominant. After the on-shell contributions are subtracted from the NLO rate for $gb \to tH^-$, we can match the two results simply by adding them, without any problem of double counting.

It is useful at this point to compare our final predictions with those published in Ref. [19]. For $m_H = 250$ GeV and $m_t = 175$ GeV, and for the same value of $\tan\beta = 30$, our predicted K factor is 1.4 versus about 1.6 in Ref. [19]. However, these numbers should not be compared directly since the factorization and the renormalization scales are different in the two calculations. In addition, there are small differences in the values of parameters such as the NLO m_b, α_s and the choices of cutoffs. If we use exactly the same parameters, cutoff choices, renormalization schemes, and most importantly the same factorization and renormalization scales, our result is 5% larger when compared to that of Ref. [19]. We attribute this 5% difference to uncertainty in the numerical integration. In the two-cutoff phase-space method, the final NLO cross section is the difference of two large quantities. The numerical uncertainty of either of the these integrations is less than 1%, but an uncertainty of 5% can develop in the difference.

There are two masses in the matrix elements that must be renormalized, m_b and m_t. The top mass m_t enters both as an external quark mass and in the Yukawa coupling. The bottom mass m_b appears only in the Yukawa coupling, since we have set the external bottom-quark mass to zero. We consistently use the on-shell (OS) scheme for

the external top-quark mass and we use the $\overline{\rm MS}$ scheme for the top and bottom quark masses in the Yukawa couplings. To understand the effect of a different renormalization scheme for top-quark mass in the Yukawa coupling, we perform our calculation in both schemes. The counterterms for the top-quark mass are

$$\frac{\delta m_t^{\overline{MS}}}{m_t} = -\frac{\alpha_s}{4\pi} C_F (4\pi)^\epsilon \Gamma(1+\epsilon) \frac{3}{\epsilon_{UV}}, \tag{7}$$

$$\frac{\delta m_t^{OS}}{m_t} = -\frac{\alpha_s}{4\pi} C_F \left(\frac{4\pi\mu^2}{m_t^2}\right)^\epsilon \Gamma(1+\epsilon)\left(\frac{3}{\epsilon_{UV}} + 4\right), \tag{8}$$

for the $\overline{\rm MS}$ and the OS scheme, respectively. Changing from one scheme to another can induce about 12% difference in the NLO cross section relative to the LO Born cross section.

We judge it physically more attractive to use the OS scheme for the external top-quark mass since the top-quark mass reconstructed in experiments is the pole mass. Nevertheless, it is perhaps best to admit that the difference in scheme choice is tantamount to a difference at the next order in α_s and thus should be viewed as a theoretical systematic uncertainty at the order of perturbation theory in which we are working.

D. Production at the Tevatron

The successful matching of the Breit-Wigner approximation and the process $gb \to tH^-$ does not apply readily at the Tevatron. In Fig. 5 we observe that the LO process $gb \to tH^-$ underestimates the cross section compared to $\bar{b}tH^-$ production [29]. At the Tevatron the gluon luminosity is not dominant in the relevant region of partonic fractional momentum x. The gluon initial state contributes only about 10% to the total $p\bar{p} \to \bar{b}tH^- + X$ rate. Because initial-state gluons are the dominant source of the bottom

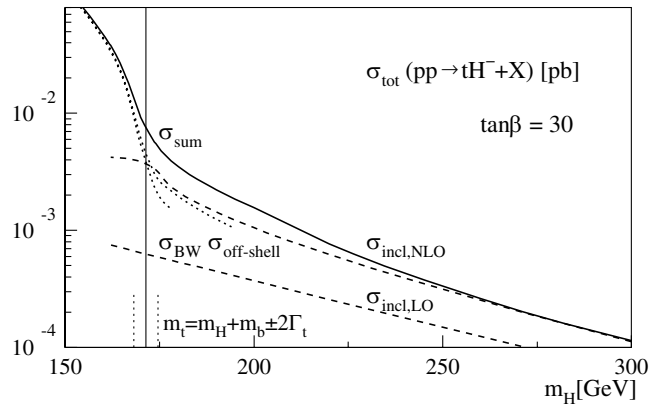

FIG. 5. The cross section for the Tevatron (2 TeV) as a function of the charged Higgs boson mass. We also show the cross sections for $pp \to t\bar{t}^* + X$ with a subsequent decay $\bar{t}^* \to \bar{b}H^-$ in the Breit-Wigner approximation and including the complete set of off-shell diagrams.

partons, we expect the leading-order gb rate to be far smaller than the true rate. The leading-order $2 \to 3$ processes contribute to the NLO gb process, and perturbation theory for the gb process is not well defined, in the sense that the NLO corrections are large. The difference between the leading-order gb rate and the off-shell $\bar{b}tH^-$ production rate is slightly less than a factor 10 because the gb rate is still enhanced by the resummation of large logarithmic terms in the bottom parton picture. We limit ourselves to LHC results for most of the rest of this paper.

The NLO inclusive tH^- rate consistently includes the whole set of quark-initiated processes, Eq. (4). Because these quark processes are dominant at Tevatron energies, the K factor for the gb process can be as large as 5 for $m_H \sim 175$ GeV. The NLO inclusive rate matches the exclusive rate from $p\bar{p} \to \bar{t}^* t + X$; $\bar{t}^* \to \bar{b}H^-$ fairly well, particularly in view of possible remaining differences between these two channels. The cross section $\sigma_{\text{off-shell}}$ for $p\bar{p} \to \bar{t}^* t + X$ is calculated at leading order and evaluated with leading-order running couplings and parton densities, while the quark-initiated contributions to the NLO inclusive rates $\sigma_{\text{incl,NLO}}$ are evaluated with NLO quantities. Moreover, the collinear divergences in the exclusive rate are regulated by a physical bottom-quark mass, while the NLO inclusive rate neglects the bottom-quark mass and is regulated by mass factorization, i.e. by subtraction of the divergent contributions to avoid double counting with the NLO evolution of the parton densities.

Just as for the LHC we see that the Breit-Wigner approximation and the complete off-shell matrix element evaluation agree very well up to $m_H \sim m_t$. Above threshold the LO gb rate is significantly smaller than the complete off-shell rate, but the NLO inclusive rate matches the exclusive rate well. The visible effect which the Breit-Wigner contribution has on the matched/added sum of the cross sections may be unexpected, but we keep in mind the substantial theoretical uncertainty on the NLO prediction. The NLO contribution from the $q\bar{q} \to \bar{b}tH^-$ production process is larger than the LO gb induced rate. The formally NLO gb induced rate enters with a much wider band of uncertainty than the 20% we quote for the perturbatively well behaved LHC process. This wider band covers different schemes for phasing out the Breit-Wigner contribution toward large Higgs boson masses. In Fig. 5 we cut off the Breit-Wigner cross sections for Higgs boson masses between 200 GeV and 250 GeV, i.e. roughly 20 top-quark widths above threshold.

Although we obtain a predicted cross section at the Tevatron for the entire range of m_H, we emphasize that the matching of the Breit-Wigner production process and gb fusion works only if we take into account the NLO corrections to the gb channel. At the LHC the same matching of the two approaches at threshold makes sense even for the leading-order $gb \to tH^-$ rate. Because the bottom parton picture is perturbatively stable at the LHC energy,

the prediction of the charged Higgs boson production rate suffers from smaller theoretical uncertainty.

III. KINEMATIC DISTRIBUTIONS

The bottom parton picture underlies the calculation of the production cross section. As summarized above, the bottom parton description provides an appropriate way to compute the total cross section for charged Higgs boson production if an appropriate bottom-quark factorization scale is used. We establish three results in extending our analysis to the kinematic distributions. The normalized distributions of sufficiently inclusive variables do not change significantly from a LO to a NLO treatment of the process $gb \to tH^-$. Second, the distributions as well as the total rate do not have a strong scale dependence. In particular, checking the limit $\mu_F \to m_b$, we verify that the bottom parton picture does not have much impact on the shape of the kinematic distributions of the heavy final-state particles. Finally, we test the approximation of vanishing bottom-quark mass in the phase space and the matrix elements.

The first statement is easy to confirm. We show the rapidity, the transverse momentum, and the invariant mass distributions for the heavy final-state particles in Fig. 6. Although the additional bottom-quark jet in the final state absorbs part of the momentum from the incoming partons, the NLO transverse momentum distributions are minimally harder. The extra NLO purely quark-initiated production process has a considerably harder p_T spectrum, but it contributes only 10% to the NLO rate (see also the quark induced contribution in the left panel of Fig. 7). For single particle spectra at the LHC, we conclude that the shift in the final-state distributions from LO to NLO is smaller than the typical scale uncertainty of 20% on the NLO rate. Similar behavior is found, for example, in the production of heavy supersymmetric particles at NLO [26,33].

A. Zero transverse momentum approximation

The transverse momentum and the rapidity distributions of the heavy final-state particles are depicted in Fig. 6. The choice of the bottom-quark factorization scale $\mu_F = M/5$ has been shown to be a part of a consistent bottom parton

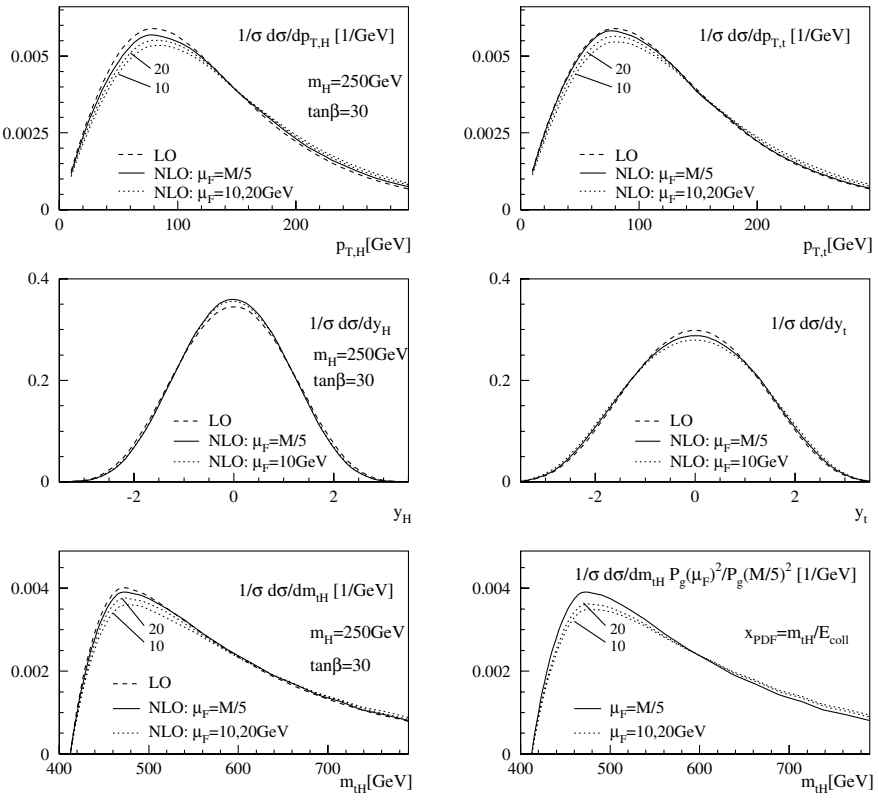

FIG. 6. The kinematic distributions for the heavy final-state particles at the LHC: transverse momentum and rapidity of the charged Higgs boson (left) and the top quark (right) for the process $gb \to tH^-$. The dashed curve shows the leading-order distribution with the central choice of scales. The solid and the dotted curves represent the NLO results for three choices of the bottom quark and the gluon factorization scale $\mu_F = M/5$, $\mu_F = 20$ GeV and $\mu_F = 10$ GeV. The bottom row shows the distribution of the invariant mass of the top quark and the Higgs boson pair from the LO and NLO calculations, plus a rescaled NLO distribution (the last panel). The scaling factor involves the gluon parton densities at the different factorization scales.

picture for this class of processes at the LHC [14–16]. It remains to be checked whether the collinear approximation for the gluon splitting into a bottom parton is appropriate for the distributions of the final-state particles.

We make use of the method described in Sec. II B to test the bottom parton approach and, in particular, the approximation of negligible transverse momentum of the incoming bottom parton. The bottom parton density vanishes if the bottom-quark factorization scale approaches the bottom-quark mass $\mu_{F,b} \to m_b$. For consistency reasons we use the same factorization scale for all partons, but neither the gluon density nor the light-quark densities change dramatically as $\mu_F \to m_b \gg \Lambda_{\rm QCD}$. In this limit the NLO gb induced cross section at the LHC is dominated by the process $gg \to \bar{b}tH^-$. Even though the final-state bottom quark is massless in the calculation, the corresponding rate is finite and well defined for any factorization scale $\mu_F > m_b$. All divergences in the $gg \to \bar{b}tH^-$ process, regulated originally by a bottom-quark mass, are absorbed into the definition of the NLO parton densities. As described in Sec. II B, when the bottom-quark factorization scale takes the limit $\mu_{F,b} \to m_b$ the physical picture shifts from the resummed cross section, including a large logarithmic term $\log p_{T,b}/m_b$, to the $\bar{b}tH^-$ situation in which the large logarithmic contribution could be removed, for example, by a detector cut $p_{T,b}^{\rm min}$. We show the difference between the NLO distributions with the central factorization scale $\mu_F = M/5$ and the small scale limit in Fig. 6. The scales we use are $\mu_F = 10, 20$ GeV. In principle, we could as well try $\mu_F = 5$ GeV, for which the calculated bottom-quark density is well defined, but the parton densities of gluons and light quarks are poorly constrained. We checked that we would then see all the features described below for scales down to 10 GeV, except that their effect on the cross sections would be numerically more pronounced.

We see in Fig. 6 that the final-state top quark and Higgs boson momentum distributions become somewhat harder when we increase the contributions from the $2 \to 3$ matrix elements, going to $\mu_F = 20$ GeV and $\mu_F = 10$ GeV. The same behavior is seen in the invariant mass of the top quark and the Higgs boson pair, m_{tH}, shown in Fig. 6. To explore this feature we present a normalized distribution of the m_{tH} invariant mass, in which we rescale the gluon distribution function for the central choice $\mu_F = M/5$ by a factor $P_g(\mu_F, x_{\rm PDF})^2/P_g(M/5, x_{\rm PDF})^2$, to estimate the effect of the parton densities. Because most of the cross section arises from production near threshold, we can approximate $x_{\rm PDF} = m_{tH}/E_{\rm coll}$ with $E_{\rm coll} = 14$ TeV. The physics motivation of this cross check is that the gluon densities become slightly harder for smaller scales, and we want to understand whether the hardening of the m_{tH} distribution arises from the shift from the bottom parton picture to the gluon fusion picture or if it is due to an overall hardening of the gluon parton spectrum. In Fig. 6 we observe that scaling the usual NLO distribution with the x dependence of the gluon parton density reproduces the hardening of the top quark and Higgs boson spectra. Concluding this argument, we find a slight shift in the spectrum at smaller factorization scales, but this shift is induced by the shape of the gluon parton density. The two sets of distributions in the bottom row of Fig. 6 show that there appears to be no problem with the bottom parton approximation for sufficiently inclusive distributions of the heavy final-state particles at the LHC. While there is a large logarithmic term $\log p_{T,b}/m_b$ present in the $\bar{b}tH^-$ production rate, no additional perturbative pitfalls appear in the gb process after the logarithmic terms are resummed. All additional dependence on the (neglected) transverse momentum of the final-state bottom jet is effectively power suppressed.

B. Zero bottom-quark mass approximation

We have compared the gb induced process with the process $gg \to \bar{b}tH^-$ without a finite bottom-quark mass in the phase space or in the matrix element. For the kinematic distributions of the bottom quarks this approximation is not obviously good. In our NLO approach the divergences in the $p_{T,b}$ spectrum are compensated by a negative infinity at $p_{T,b} = 0$, i.e. in the $2 \to 2$ kinematic limit. This distribution is not physical, and all-orders soft-gluon resummation should be taken into account [34] to obtain a physical spectrum with a peak at some small value of $p_{T,b}$. With the bottom-quark mass as a regulator, the $p_{T,b}$ spectrum peaks near m_b [14]. However, when the gb process is used, we are implicitly not interested in observing the final bottom-quark jet and in its distributions; rather, we are interested in the distributions of the heavy final-state particles. In Fig. 7 we show the normalized transverse momentum distribution of the top quark for the gb process at NLO, and for the $2 \to 3$ process, with two different cutoffs: one with the physical bottom-quark mass and the other with a smaller mathematical cutoff (we use $1/10$ of the bottom-quark pole mass). We observe that the gb calculation agrees with the $2 \to 3$ matrix element approach with the physical bottom-quark mass. The curve with a smaller cutoff instead of the bottom-quark mass agrees perhaps too well with the NLO process in which the bottom-quark mass is neglected. The distribution in the invariant mass of the tH^- final state confirms this level of agreement. The dependence on the bottom-quark mass seems to be power suppressed, and the approximation of zero bottom-quark mass is justified.

There are limitations of our argument for charged Higgs boson production at the Tevatron. The $2 \to 3$ rate with a finite bottom-quark mass, induced by incoming quarks, shows considerably harder momenta of final-state top quarks. While the total cross section is predicted correctly in the bottom parton picture, this effect might mean that the kinematic distributions require more careful study at Tevatron energies. The effect is not related to the approxi-

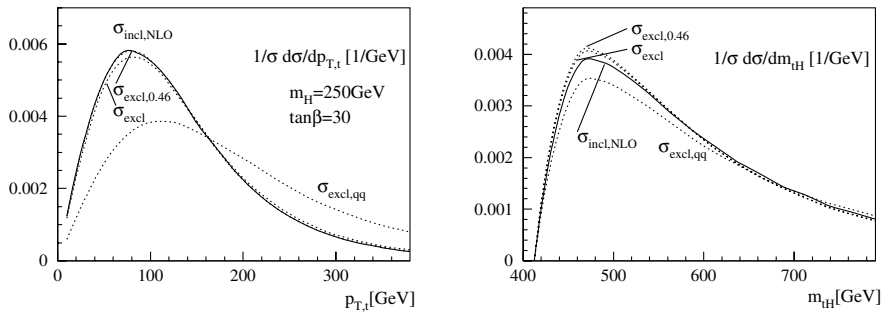

FIG. 7. The kinematic distributions for the final state at the LHC: the top-quark transverse momentum and the invariant mass of the top quark and the Higgs boson pair. We compare the NLO result for the process $gb \to tH^-$ with the process $pp \to \bar{b}tH^- + X$. Apart from the complete set of diagrams with the physical bottom-quark mass, we show the purely $q\bar{q}$ induced process and the complete set of diagrams with a mathematical cutoff instead of the physical bottom-quark mass $m_b \to 0.46$ GeV.

mation of zero bottom-quark mass. Instead, it probes the perturbative link between the contribution of gluon and quark-initiated diagrams in the $2 \to 3$ production processes and the bottom parton description.

Finally, we remark that the total cross section and the inclusive distributions of the final-state particles are correctly predicted in the bottom parton picture. Neither the small transverse momentum approximation nor the small bottom-quark mass approximation in the bottom parton picture has a visible effect on the transverse momentum, the rapidity, and the invariant mass distributions of the final-state top quark and Higgs boson. Shifts induced by the massless bottom parton approximation are washed out once detector resolution is taken into account. For the processes under consideration, the contribution from the $q\bar{q}$ initial states is less important at the LHC than at the Tevatron. The light-quark induced subprocesses show harder transverse momentum spectra, a difference that should be considered for predictions at Tevatron energies.

C. Final-state correlations

The fully differential nature of the two-cutoff method enables us to place a kinematic cut on one final-state particle and to study the distribution in the momentum of other particles in the final state. It allows us to examine any correlation observable among the final-state particles which does not spoil the cancellation of soft and (initial state) collinear divergences. For reasons of acceptance and/or to improve signal purity with respect to backgrounds, it may be helpful to make final-state cuts that act in a similar fashion to a cut on the transverse momentum of the top quark. If the charged Higgs boson decays to a τ-lepton jet, a simple transverse momentum cut on a lepton from the top-quark decay could be an example. We examine in this section how such a selection may affect the expected transverse momentum distribution of the Higgs boson. The Higgs boson transverse momentum distribution is crucial because it determines the boost of the Higgs boson decay products. If these products include bottom-quark or τ-lepton jets, their transverse momentum distributions determine the tagging efficiencies.

The topology of the final state and the correlation in momentum between the top quark and the Higgs boson change once NLO corrections are included. Instead of a back-to-back pair of heavy states at leading order, the NLO topology includes three final-state particles sharing the total transverse momentum. In Fig. 8, we show the $p_{T,H}$ distributions after the cuts $p_{T,t} > 50$ GeV or $p_{T,t} > 100$ GeV. At LO, a cut on $p_{T,t}$ indeed eliminates values of $p_{T,H}$ below this cut. The LO distribution $d\sigma/dp_{T,H}$ in the range $p_{T,H} > 100$ GeV is identical for the two cases shown: $p_{T,t}^{\min} = 50$ GeV and $p_{T,t}^{\min} = 100$ GeV. At NLO, the figure shows that the effects of cuts on the momentum of one final-state particle extend over a significant range in the momentum of another final-state particle. Owing to the presence of the final-state jet, the NLO transverse momentum distribution of the Higgs boson extends all the way to zero, as shown in Fig. 8. The impact of the $p_{T,t}$ cut on the NLO distributions is evident well above $p_{T,H} = p_{T,t}^{\min}$, and the distributions do not coincide until $p_{T,H} > 200$ GeV. The ratio of the NLO and LO distributions cannot be represented by a simple correction (or "K") factor. This factor would be infinite for values of $p_{T,H}$ less than the value of the cut on $p_{T,t}$, less than unity in a small interval where $p_{t,H}$ is just above the cut, and uniformly greater than unity for $p_{T,H} > 1.5 p_{T,t}^{\min}$.

In contrast to the differences seen in Fig. 8, the effect of a $p_{T,t}$ cut on the Higgs boson rapidity distribution is trivial: the NLO rapidity distributions of the Higgs boson and the top quark are reduced by an approximately uniform factor.

The distribution in $p_{T,H}$ is well defined at NLO. The soft and the initial-state collinear divergences appear with Born-type kinematics, just like the explicit infrared poles. However, we expect strong cancellations between large NLO negative virtual contributions and positive NLO real emission contributions at the LO threshold. Numerical problems can arise once these cancellations yield a cross section at threshold that is more than an order

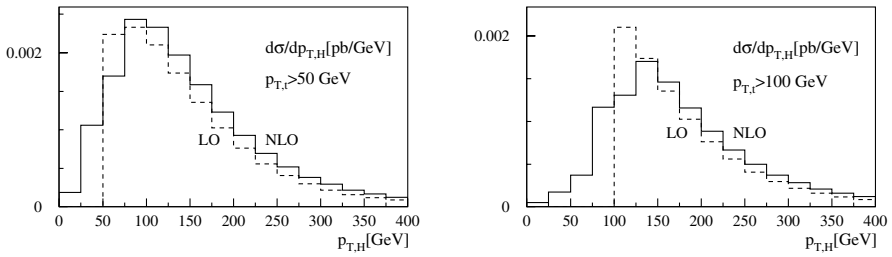

FIG. 8. LO and NLO p_T distribution of the Higgs boson, with cuts $p_{T,t} > 50$ GeV or $p_{T,t} > 100$ GeV on the transverse momentum of the top quark. The Higgs boson mass is $m_H = 250$ GeV, and $\tan\beta = 30$.

of magnitude smaller than the contributing parts. Motivated by evidence of instability in the threshold region $p_{T,H} = p_{T,t}^{\rm cut}$ if we use the values of δ_s and δ_c chosen earlier, we select cutoff values $\delta_s = 10^{-2}$ and $\delta_c = 2 \times 10^{-4}$ to obtain the results shown in Fig. 8. These relatively large values of the cutoffs remain in the safe region for the total cross section, as shown in Fig. 2. Moreover, we use fairly wide bins, to be less sensitive to numerical cancellations in the threshold region. The behavior of the curves in Fig. 8 near threshold indicates some remaining uncertainty, so the $p_{T,H}$ distributions should be taken with reservation at threshold. They should be reliable one bin or more from threshold in each direction.

Another distribution of interest is the vector sum of the transverse momenta of the top quark and the Higgs boson ($\Sigma p_T = |(\vec{p}_{T,t} + \vec{p}_{T,H})|$) shown in the left panel of Fig. 9. The LO distribution is a single peak at $\Sigma p_T = 0$ since the top quark and the Higgs boson balance in transverse momentum at this order. At NLO, the observable Σp_T is the transverse momentum of the third jet in the final state. The shape of the distribution depends only mildly on the Higgs boson mass. The NLO distribution in Σp_T shows a marked divergence as $\Sigma p_T \to 0$. This divergence reflects a limitation of our fixed-order calculation and points to the eventual need for all-orders resummation of the effects of soft-gluon radiation, as discussed and implemented for other processes [34].

The right panel of Fig. 9 displays the two-dimensional correlation between Σp_T and $\Delta\phi = |\phi_t - \phi_H|$ for the sum of all $2 \to 3$ contributions to the cross section. Here $\Delta\phi$ is the difference between the azimuthal angles of the Higgs boson and the top quark. At LO it is fixed to $\Delta\phi = \pi$, but for the $2 \to 3$ processes the distribution extends to all $\Delta\phi$, again a manifestation of the fact that an additional parton in the final state contributes to the transverse momentum balance. It is interesting to see that the Σp_T distribution for $\Delta\phi \neq \pi$, i.e. for a topology different from LO, develops a maximum for $\Sigma p_T \sim 50$ GeV and drops to zero for $\Sigma p_T \to 0$. This feature and the corresponding behavior of $\Delta\phi$ for $\Sigma p_T \neq 0$ reflect the fact that the (resummable) divergence is limited to the LO topology.

IV. SUPERSYMMETRIC CONTRIBUTIONS

Supersymmetric diagrams contribute to the production rate for $gb \to tH^-$ at the same level as the NLO QCD contributions ($\alpha_s^2 y_{b,t}^2$). These diagrams are virtual gluon exchange diagrams, where the gluons and quarks are replaced by their supersymmetric partners, gluinos and squarks. A feature of squarks is the mixing between the supersymmetric partners of the left-handed and the right-handed quarks. The 2×2 bottom-squark mass matrix has an off-diagonal entry $m_b(A_b - \mu \tan\beta)$, and the top-squark mass matrix has an entry $m_t(A_t - \mu/\tan\beta)$. Here μ is the Higgsino mass parameter which links the two Higgs doublets in the Lagrangian, and A_i is the trilinear squark-squark-Higgs boson coupling parameter. The off-diagonal entry in the matrix element is proportional to the mass of the standard model partner, and it is usually neglected for the first and second generations. For large values of $\tan\beta$ bottom-squark mixing can become larger than top-squark mixing.

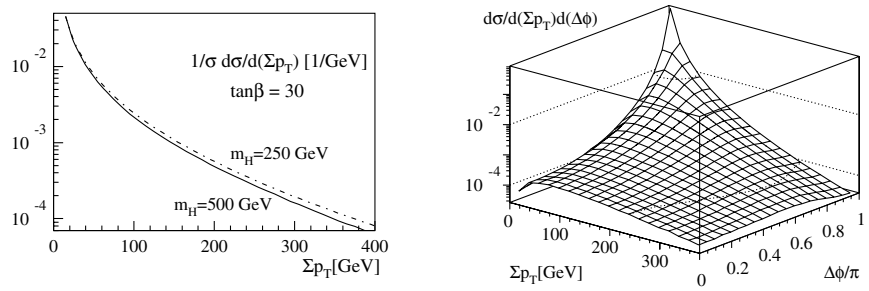

FIG. 9. Left: Normalized distributions in Σp_T (defined in the text) for the NLO process $gb \to tH^-$, for $m_H = 250$ GeV and 500 GeV. Right: A two-dimensional plot of the correlation between Σp_T and $\Delta\phi$, for $m_H = 250$ GeV and $\tan\beta = 30$.

In the limit of large $\tan\beta$, the leading supersymmetric contributions are not loop diagrams, but renormalization terms [35]. This point becomes evident if we compute the corrections to the btH^- vertex in the limit of vanishing bottom-quark mass, but finite bottom-quark Yukawa coupling. This approach is justified from a formal point of view because the connection between the mass and the Yukawa coupling is a property of electroweak symmetry breaking and not protected once the symmetry is broken. Disassociation of the mass and the Yukawa coupling becomes apparent in a type-II two-Higgs-doublet model like the MSSM. Because the bottom-quark Yukawa coupling always appears as $m_b \tan\beta$, the relationship between the mass and the Yukawa coupling is not fixed. If we compute the renormalization of the tbH^- vertex with a zero external bottom-quark mass, bottom-squark mixing diagrams lead to contributions which look like mass renormalization terms, i.e. terms which create a finite bottom-quark mass in the external leg. However, this interpretation cannot be correct, since mass renormalization has to be multiplicative. Instead, we see that these renormalization factors describe a misalignment of the bottom-quark Yukawa coupling and the bottom-quark mass, which appears for zero bottom-quark mass as well as for finite values. In complete analogy to a mass renormalization, these coupling renormalization diagrams can be resummed to all orders and lead to a correction [36]:

$$\frac{m_b \tan\beta}{v} \to \frac{m_b \tan\beta}{v} \frac{1}{1+\Delta_b},$$

$$\Delta_b = \frac{\sin(2\theta_b)}{m_b} \frac{\alpha_s}{4\pi} C_F m_{\tilde{g}} \frac{1}{i\pi^2} [B(0, m_{\tilde{b},2}, m_{\tilde{g}}) - B(0, m_{\tilde{b},1}, m_{\tilde{g}})] = \frac{\alpha_s}{2\pi} C_F m_{\tilde{g}} (-A_b + \mu \tan\beta) I(m_{\tilde{b},1}, m_{\tilde{b},2}, m_{\tilde{g}}) \tag{9}$$

$$I(a,b,c) = -\frac{1}{(a^2-b^2)(b^2-c^2)(c^2-a^2)} \left[a^2 b^2 \log\frac{a^2}{b^2} + b^2 c^2 \log\frac{b^2}{c^2} + c^2 a^2 \log\frac{c^2}{a^2} \right].$$

The function $B(p^2, m_1, m_2)$ is the usual scalar two-point function; $C_F = 4/3$ is the Casimir factor in the fundamental representation of $SU(3)$. There are similar additional terms proportional to the strong coupling or to the top-quark Yukawa coupling, but Eq. (9) is the leading contribution for large $\tan\beta$.

Since these Δ_b corrections are the leading $\tan\beta$-enhanced supersymmetric contributions to the production cross section, and since the charged Higgs boson search is most promising at $\tan\beta \gtrsim 15$, we might speculate that these corrections to the $gb \to tH^-$ production rate are sufficient. Equation (9) shows that the shift in the Yukawa coupling can have large effects [37] provided that $\mu \tan\beta$ is large (preferably negative), the gluino mass is large, and bottom-squark masses are not too large. In this limit the percentage corrections are approximately $\Delta_b \sim \mu \tan\beta / m_{\tilde{g}}$. The non-$\Delta_b$-type supersymmetric corrections are negligible compared, for example, to the remaining NLO scale variation.

TABLE I. Supersymmetric corrections to the production cross section $gb \to tH^-$ from nonresummed and resummed Δ_b corrections, Eq. (4), and from the explicit remaining supersymmetric loop diagrams. The supersymmetric parameter points are chosen according to the benchmarks in Ref. [38]. All masses are given in units of GeV. The percentage changes are defined with respect to the purely gluonic NLO rates.

mSUGRA	m_H	$\tan\beta$	m_0	$m_{1/2}$	A_0			μ	$\sigma_{\rm LO}$ [fb]	$\sigma_{\rm NLO}$ [fb]	Δ_b	$\Delta_b^{\rm resum}$	non-Δ_b
1a	402	10	100	250	−100			352	18.7	25.6	−11.0%	−10.2%	−1.9%
1b	543	30	200	400	0			501	47.1	61.7	−27.9%	−23.5%	−4.6%
2	1446	10	1450	300	0			125	0.09	0.13	−0.92%	−0.91%	−1.7%
3	578	10	90	400	0			509	5.81	8.02	−10.1%	−9.5%	−1.1%
4	416	50	400	300	0			377	304	395	−39.0%	−31.0%	−4.6%
5	699	5	150	300	−1000			640	3.73	5.73	−8.5%	−8.0%	0.8%
mSUGRA-like			m_0	$m_{1/2}$	A_0	M_1	$M_{2,3}$						
6	470	10	150	300	0	480	300	394	11.6	16.0	−10.2%	−9.5%	−1.3%
GMSB			Λ	$M_{\rm mes}$	$N_{\rm mes}$								
7	387	15	40×10^3	80×10^3	3			300	36.5	48.0	−8.5%	−8.1%	−0.9%
8	521	15	100×10^3	200×10^3	1			398	15.0	20.4	−7.5%	−7.1%	−0.5%
AMSB			m_0	$m_{\rm aux}$									
9	916	10	400	60×10^3				870	0.92	1.29	−10.6%	−9.9%	4.1%

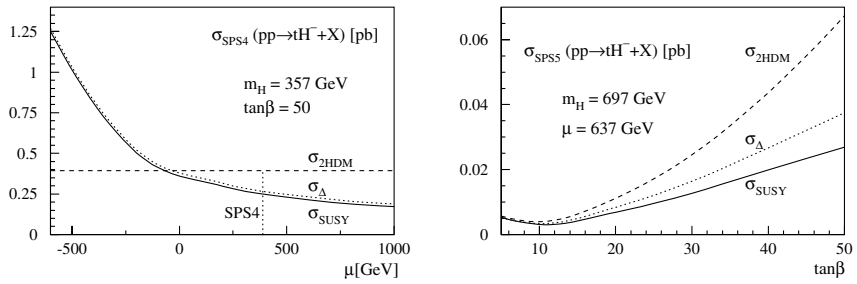

FIG. 10. The supersymmetric contributions to the NLO cross section for $gb \to tH^-$, with the dotted curve showing the resummed Δ_b contribution and the solid curve showing the combination of the resummed Δ_b and non-Δ_b contributions. The supersymmetric parameters are described in Table I. The central value of μ in SPS4 is noted in the plot; the central value of $\tan\beta$ in SPS5 is at the lower end of the plot, $\tan\beta = 5$. All parameters and masses except for μ and $\tan\beta$ are kept constant. The curves denoted $\sigma_{\rm 2HDM}$ show NLO QCD cross sections without SUSY contributions.

The supersymmetric contributions to the charged Higgs boson production cross sections are shown in Table I for the SPS [38] parameters. The contributions are split into the Δ_b corrections, as defined in Eq. (9), and the remaining supersymmetric diagrams. We present the Δ_b contributions in the NLO version $1 - 2\Delta_b$ as well as after resummation, $1/(1 + \Delta_b)^2$. The ratios of the SUSY corrections to the NLO QCD cross sections are given in the last three columns. The negative sign of the Δ_b contributions is fixed by the sign of μ. The sign of μ is a free parameter, linked to SUSY contributions to the transition rate $b \to s\gamma$. In this process the measured rate is consistent with the standard model prediction. There are additional charged Higgs boson and chargino induced contributions in the MSSM. For $\mu > 0$ they enter with opposite signs and therefore tend to cancel numerically, while for $\mu < 0$, in particular, in the mSUGRA supersymmetry breaking scheme, the parameter space is closely constrained. Therefore, all SPS points are chosen with positive sign of μ.

In Table I we observe that the Δ_b corrections are dominant for all points with $\tan\beta \geq 15$, particularly for the two points with $\tan\beta = 30, 50$. The leading contribution for large $\tan\beta$ is described correctly by the Δ_b corrections. At maximum, all supersymmetric corrections are of the order of the remaining scale variation and our estimate of the theoretical uncertainty of 20%, as long as $\tan\beta \lesssim 30$. This modest correction is not necessarily true for the entire supersymmetric parameter space, and the Δ_b corrections can be much larger [37]. However, the small correction reflects the ansatz used in supersymmetry breaking. None of the scenarios in Table I is designed to produce a large splitting in the supersymmetric mass parameters at the weak scale or a large value of $|\mu|$, which would favor large Δ_b-type corrections. In general, large values of $|\mu|$ are a challenge in high-scale motivated models. For fine-tuning reasons these models usually produce $|\mu|$ of order the weak scale, to avoid large cancellations of different renormalization group contributions to the value of m_Z. Even in the focus-point [39] inspired SPS2 the contribution to weak-scale parameters that are proportional to m_0 cancels in itself, decoupling the value of m_0 from the leading renormalization group running. All other parameters remain at typical weak-scale values. In all three SUSY breaking scenarios considered, the large gluino mass, linked to the relative dominance of the corresponding beta function β_3, is the reason the Δ_b correction is not negligible.

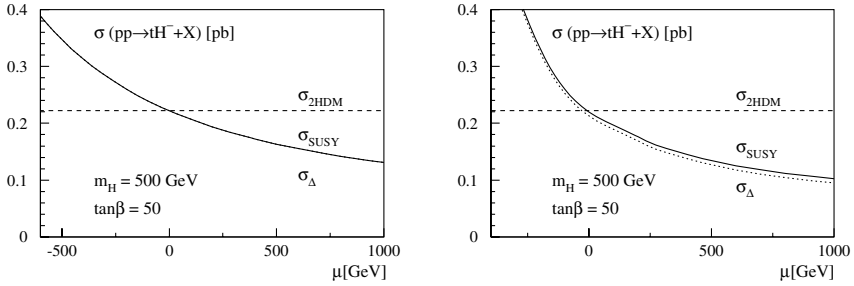

FIG. 11. The supersymmetric contributions to the NLO prediction for the cross section $gb \to tH^-$. The supersymmetric parameter points are the scenarios A and C, picked from Ref. [37]. All parameters and masses except for μ are kept constant. The gluino mass in both scenarios is 1 TeV; the lighter top-squark and bottom-squark masses are 0.5 TeV for scenario A (left-hand side) and 1 TeV for scenario C (right-hand side). The top-squark mass difference is 100 GeV and the bottom-squark mass difference 150 GeV. In contrast to Ref. [37] we resum only the SUSY-QCD corrections. The curves denoted $\sigma_{\rm 2HDM}$ show NLO QCD cross sections without SUSY contributions.

In Fig. 10 we show that the Δ_b contributions can become large once we depart from the unification scenarios. Starting from the mSUGRA motivated points SPS4 and SPS5, listed in Table I, we vary μ and $\tan\beta$, leaving all other masses and parameters invariant. As expected, the nonresummed Δ_b corrections become arbitrarily large for large values of $|\mu|$, and the resummed Δ_b correction can become arbitrarily large for some negative values of μ, both limited only perturbatively and ultimately by unitarity of the enhanced bottom-quark Yukawa coupling. The sign of the Δ_b correction is fixed by the sign of μ, and the remaining SUSY contributions are small. For comparison, we also show the NLO cross sections without SUSY contributions included, the typical case for a two-Higgs-doublet model (2HDM). These curves are labeled σ_{2HDM}. The NLO QCD cross section does not depend on the SUSY parameter μ, but it increases as $\tan\beta$ gets large, as expected. In Fig. 11 we show the same effect, starting from the scenarios A and C in Ref. [37]. Because the value of $\tan\beta = 50$ is large, the non-Δ_b corrections are completely negligible, while the Δ_b corrections can become arbitrarily large. The difference in the size of the corrections in the two panels of Fig. 11 can be understood from Eq. (9) in the limit $a \sim b$ for the bottom-squark masses and either $c \gg a, b$ or $c \sim a, b$. In both cases the Δ_b corrections are suppressed by the heaviest mass in the system, i.e. the gluino mass, but the prefactor is larger if all masses involved are of the same order.

V. CONCLUSIONS

We evaluate the inclusive and differential cross sections for the associated production of a top quark along with a charged Higgs boson at Tevatron and LHC energies to next-to-leading order in QCD and in supersymmetric QCD.

Using the two-cutoff scheme to treat the soft and collinear singularities, we find stable results for total and differential cross sections over large ranges of the cutoff parameters as well as of the factorization and renormalization scales. While the QCD corrections to the total rate are sizable at the LHC, $K \sim 1.4$ [14], the shifts in the normalized kinematic distributions of the heavy final-state top quark and Higgs boson are negligible. The scale dependence gives us a reasonable estimate of about 20% on the remaining theoretical uncertainty.

In the regime where $m_H < m_t$, we compute the NLO cross section by subtracting the intermediate on-shell divergences in the narrow width approximation. This procedure allows us to match the NLO cross section for the process $gb \to tH^-$ with the contributions from $gg \to t\bar{t}^*$ with a subsequent decay $\bar{t}^* \to \bar{b}H^-$, simply by adding the rates. This method yields a prediction for the cross section for associated charged Higgs boson production over the entire range of Higgs boson.

At the Tevatron, charged Higgs boson production is likely to be observed only for small masses of the Higgs boson. In this regime we show the validity of the Breit-Wigner approximation in the $t\bar{t}$ production process. We can add the off-shell production rate at NLO.

Examining the NLO momentum distributions for inclusive charged Higgs boson production, we show the validity of the bottom parton description beyond the total rate. Neither the collinear phase-space approximation nor the approximation of zero bottom-quark mass has a visible impact on the kinematic distributions of the heavy final-state particles.

The fully differential nature of the two-cutoff method enables us to place a kinematic cut on one final-state particle and study the distribution in momentum of the other particles. It allows us also to examine momentum correlations among the final-state particles.

We explore the effects of virtual supersymmetric particles in NLO loop diagrams and find that the universal Δ_b corrections to the Yukawa coupling can be sizable. In the two-Higgs-doublet model, the remaining explicit loop contributions to the NLO rate are below the level of the scale uncertainty.

ACKNOWLEDGMENTS

We thank Brian Harris for his assistance with the two-cutoff method and Shouhua Zhu for providing comparisons between our results and those in Ref. [19]. We are grateful for helpful discussions with Carlos Wagner and John Campbell. J. J. acknowledges helpful conversations with Jungil Lee. T. P. wants to thank Sasha Nikitenko for his support and for pointing out questions from the experimental community. Moreover, T. P. wishes to thank Thomas Teubner and Sakis Dedes for helpful discussions, and last but not least the IPPP in Durham for their kind hospitality during the final stage of this paper. The research of E. L. B. and J. J. in the High Energy Physics Division at Argonne National Laboratory is supported by the U.S. Department of Energy, Division of High Energy Physics, under Contract No. W-31-109-ENG-38. T. H. is supported in part by the DOE under Grant No. DE-FG02-95ER40896, and in part by the Wisconsin Alumni Research Foundation.

[1] D. Abbaneo *et al.*, hep-ex/0212036.

[2] CMS Collaboration, Technical Proposal No. CERN/

LHCC/94-38; ATLAS Collaboration, Technical Proposal No. CERN/LHCC/94-43.

[3] T. Plehn, D. Rainwater, and D. Zeppenfeld, Phys. Lett. B **454**, 297 (1999).

[4] U. Baur, T. Plehn, and D. L. Rainwater, Phys. Rev. D **69**, 053004 (2004).

[5] F. Abe *et al.* (CDF Collaboration), Phys. Rev. Lett. **79**, 357 (1997); B. Abbott *et al.* (D0 Collaboration), Phys. Rev. Lett. **82**, 4975 (1999).

[6] E. Eichten, I. Hinchliffe, K. D. Lane, and C. Quigg, Rev. Mod. Phys. **56**, 579 (1984); **58**, 1065 (1986); N. G. Deshpande, X. Tata, and D. A. Dicus, Phys. Rev. D **29**, 1527 (1984).

[7] J. F. Gunion, H. E. Haber, F. E. Paige, W. K. Tung, and S. S. Willenbrock, Nucl. Phys. **B294**, 621 (1987); A. Krause, T. Plehn, M. Spira, and P. M. Zerwas, Nucl. Phys. **B519**, 85 (1998); A. A. Barrientos Bendezu and B. A. Kniehl, Nucl. Phys. **B568**, 305 (2000); O. Brein and W. Hollik, Eur. Phys. J. C **13**, 175 (2000).

[8] D. A. Dicus, J. L. Hewett, C. Kao, and T. G. Rizzo, Phys. Rev. D **40**, 787 (1989); A. A. Barrientos Bendezu and B. A. Kniehl, Phys. Rev. D **59**, 015009 (1999); **63**, 015009 (2001); O. Brein, W. Hollik, and S. Kanemura, Phys. Rev. D **63**, 095001 (2001).

[9] W. Hollik and S. H. Zhu, Phys. Rev. D **65**, 075015 (2002).

[10] R. M. Barnett, H. E. Haber, and D. E. Soper, Nucl. Phys. **B306**, 697 (1988); A. C. Bawa, C. S. Kim, and A. D. Martin, Z. Phys. C **47**, 75 (1990); V. D. Barger, R. J. Phillips, and D. P. Roy, Phys. Lett. B **324**, 236 (1994).

[11] K. A. Assamagan, Y. Coadou, and A. Deandrea, Eur. Phys. J. direct C **4**, 1 (2002); P. Salmi, R. Kinnunen, and N. Stepanov, hep-ph/0301166; K. A. Assamagan and N. Gollub, Eur. Phys. J. C **39S2**, 25 (2005).

[12] K. A. Assamagan and Y. Coadou, Acta Phys. Pol. B **33**, 707 (2002); R. Kinnunen and A. Nikitenko, report CMS note 2003/006.

[13] J. C. Collins and W. K. Tung, Nucl. Phys. **B278**, 934 (1986); M. A. Aivazis, J. C. Collins, F. I. Olness, and W. K. Tung, Phys. Rev. D **50**, 3102 (1994); F. I. Olness and W. K. Tung, Nucl. Phys. **B308**, 813 (1988); M. Krämer, F. I. Olness, and D. E. Soper, Phys. Rev. D **62**, 096007 (2000).

[14] T. Plehn, Phys. Rev. D **67**, 014018 (2003).

[15] E. Boos and T. Plehn, Phys. Rev. D **69**, 094005 (2004).

[16] F. Maltoni, Z. Sullivan, and S. Willenbrock, Phys. Rev. D **67**, 093005 (2003); S. Dawson, C. B. Jackson, L. Reina, and D. Wackeroth, Phys. Rev. Lett. **94**, 031802 (2005).

[17] S. Dittmaier, M. Kramer, and M. Spira, Phys. Rev. D **70**, 074010 (2004); J. Campbell *et al.*, hep-ph/0405302.

[18] R. V. Harlander and W. B. Kilgore, Phys. Rev. D **68**, 013001 (2003); S. Dawson, C. B. Jackson, L. Reina, and D. Wackeroth, Phys. Rev. Lett. **94**, 031802 (2005).

[19] S. H. Zhu, Phys. Rev. D **67**, 075006 (2003).

[20] G. P. Gao, G. R. Lu, Z. H. Xiong, and J. M. Yang, Phys. Rev. D **66**, 015007 (2002).

[21] H. L. Lai *et al.* (CTEQ Collaboration), Eur. Phys. J. C **12**, 375 (2000).

[22] Y. L. Dokshitzer, Sov. Phys. JETP **46**, 641 (1977) [Zh. Eksp. Teor. Fiz. **73**, 1216 (1977)]; V. N. Gribov and L. N. Lipatov, Sov. J. Nucl. Phys. **15**, 438 (1972) [Yad. Fiz. **15**, 781 (1972)]; G. Altarelli and G. Parisi, Nucl. Phys. **B126**, 298 (1977).

[23] See, e.g., H. Baer, J. Ohnemus, and J. F. Owens, Phys. Rev. D **40**, 2844 (1989); Phys. Lett. B **234**, 127 (1990); Phys. Rev. D **42**, 61 (1990); U. Baur, T. Han, and J. Ohnemus, Phys. Rev. D **48**, 5140 (1993); **51**, 3381 (1995); **53**, 1098 (1996).

[24] B. W. Harris and J. F. Owens, Phys. Rev. D **65**, 094032 (2002).

[25] R. K. Ellis, D. A. Ross, and A. E. Terrano, Nucl. Phys. **B178**, 421 (1981); Z. Kunszt and D. E. Soper, Phys. Rev. D **46**, 192 (1992); M. L. Mangano, P. Nason, and G. Ridolfi, Nucl. Phys. **B373**, 295 (1992); S. Catani and M. H. Seymour, Nucl. Phys. **B485**, 291 (1997); **B510**, 503(E) (1998); S. Catani, S. Dittmaier, M. H. Seymour, and Z. Trocsanyi, Nucl. Phys. **B627**, 189 (2002).

[26] W. Beenakker, R. Höpker, M. Spira, and P. M. Zerwas, Nucl. Phys. **B492**, 51 (1997); W. Beenakker, M. Klasen, M. Krämer, T. Plehn, M. Spira, and P. M. Zerwas, Phys. Rev. Lett. **83**, 3780 (1999); A. Alves, O. Eboli, and T. Plehn, Phys. Lett. B **558**, 165 (2003).

[27] W. Beenakker, M. Krämer, T. Plehn, M. Spira, and P. M. Zerwas, Nucl. Phys. **B515**, 3 (1998).

[28] S. Narison, Phys. Lett. B **341**, 73 (1994).

[29] F. Borzumati, J. L. Kneur, and N. Polonsky, Phys. Rev. D **60**, 115011 (1999).

[30] U. Baur and D. Zeppenfeld, Phys. Rev. Lett. **75**, 1002 (1995).

[31] E. L. Berger and H. Contopanagos, Phys. Lett. B **361**, 115 (1995); E. L. Berger and H. Contopanagos, Phys. Rev. D **54**, 3085 (1996); E. L. Berger and H. Contopanagos, Phys. Rev. D **57**, 253 (1998).

[32] S. Catani, M. L. Mangano, P. Nason, and L. Trentadue, Phys. Lett. B **378**, 329 (1996); R. Bonciani, S. Catani, M. L. Mangano, and P. Nason, Nucl. Phys. **B529**, 424 (1998).

[33] E. L. Berger, M. Klasen, and T. Tait, Phys. Lett. B **459**, 165 (1999); E. L. Berger, M. Klasen, and T. M. P. Tait, Phys. Rev. D **62**, 095014 (2000); E. L. Berger, M. Klasen, and T. M. P. Tait, Phys. Rev. D **67**, 099901 (2003).

[34] J. C. Collins, D. E. Soper, and G. Sterman, Nucl. Phys. **B250**, 199 (1985); E. L. Berger and J. W. Qiu, Phys. Rev. D **67**, 034026 (2003), and many references cited therein.

[35] L. J. Hall, R. Rattazzi, and U. Sarid, Phys. Rev. D **50**, 7048 (1994); M. Carena, M. Olechowski, S. Pokorski, and C. E. Wagner, Nucl. Phys. **B426**, 269 (1994); A. Belyaev, D. Garcia, J. Guasch, and J. Sola, Phys. Rev. D **65**, 031701 (2002).

[36] M. Carena, D. Garcia, U. Nierste, and C. E. Wagner, Nucl. Phys. **B577**, 88 (2000); J. Guasch, P. Hafliger, and M. Spira, Phys. Rev. D **68**, 115001 (2003).

[37] A. Belyaev, D. Garcia, J. Guasch, and J. Sola, J. High Energy Phys. 06 (2002) 059.

[38] B. C. Allanach *et al.*, in *Proceedings of the APS/DPF/DPB Summer Study on the Future of Particle Physics, Snowmass, 2001*, edited by N. Graf [Eur. Phys. J. C **25**, 113 (2002)]; N. Ghodbane and H. U. Martyn, in *Proceedings of the APS/DPF/DPB Summer Study on the Future of Particle Physics, Snowmass, 2001*, edited by N. Graf.

[39] M. Drees and S. P. Martin, hep-ph/9504324; J. L. Feng, K. T. Matchev, and T. Moroi, Phys. Rev. D **61**, 075005 (2000).